

The Nuclear Outflows and Feedback in the Seyfert 2 Galaxy Markarian 573¹K. Schlesinger, Richard W. Pogge², Paul Martini²*Department of Astronomy; The Ohio State University; 140 W. 18th Avenue, Columbus, OH 43210; kschles@astronomy.ohio-state.edu*

Joseph C. Shields

Physics & Astronomy Department; Ohio University; Athens, OH 45701

Dale Fields

*Department of Physics and Planetary Sciences; Pierce College; Woodland Hills, California 91371***ABSTRACT**

We present a study of outflow and feedback in the well-known Seyfert 2 galaxy Markarian 573 using high angular resolution long-slit spectrophotometry obtained with the *Hubble Space Telescope* Imaging Spectrograph (STIS). Through analysis of the kinematics and ionization state of a biconical outflow region emanating from the nucleus, we find that the outflow does not significantly accelerate the surrounding host-galaxy interstellar gas and is too weak to be a strong ionization mechanism in the extended emission regions. Instead, the excitation of the extended regions is consistent with photoionization by the active nucleus. From energetics arguments we show that the nuclear outflow is slow and heavy and has a mechanical luminosity that is only $\sim 1\%$ of the estimated bolometric luminosity of the system. The energy in the outflow is able to mildly shape the gas in the extended regions but appears to be insufficient to unbind it, or even to plausibly disrupt star formation. These results are at odds with the picture of strong AGN feedback that has been invoked to explain certain aspects of galaxy evolution.

Subject headings: ISM: jets and outflows – galaxies: individual (Mrk 573) – galaxies: jets – galaxies: kinematics and dynamics – galaxies: Seyfert

¹Based on observations with the NASA/ESA *Hubble Space Telescope* obtained at the the Space Telescope Science Institute, which is operated by the Association of Universities for Research in Astronomy, Incorporated, under NASA contract NAS5-26555.

²Center for Cosmology and AstroParticle Physics; The Ohio State University; 191 West Woodruff Avenue; Columbus, OH 43210

1. Introduction

Recent studies of galaxy evolution have invoked a significant component of energetic feedback from an Active Galactic Nucleus (AGN) to attempt to explain many of the observed properties of galaxies. Specifically, AGN feedback has been implicated as the primary cause behind the differences between observed and theoretical galaxy luminosity functions, the observed color bimodality of galaxies (White & Frenk 1991; Springel 2000; Benson et al. 2003; Granato et al. 2004; Kauffmann et al. 2004; Springel et al. 2005a) in which galaxies are divided into distinct populations of blue star-forming galaxies and red dead galaxies (e.g. Strateva et al. 2001) with a pronounced deficit of galaxies with intermediate color, and the very tight correlations observed between the masses of supermassive black holes and their host galaxy spheroid’s velocity dispersion (Ferrarese & Merritt 2000; Gebhardt et al. 2000) and luminosity (Marconi & Hunt 2003). The relative lack of galaxies with intermediate star formation rates suggests that star formation ceases abruptly rather than gradually (Bell et al. 2004), while the tight correlations of black hole masses with the properties of their host bulges are taken as evidence that the two are strongly co-eval. In the various proposed feedback scenarios, the supermassive black holes grow primarily by accretion until they become sufficiently massive and energetic that thermal and/or radiative feedback from their activity either heats the surrounding interstellar gas or mechanically pushes it out of the host galaxy (Crenshaw et al. 2003; Begelman 2004). This simultaneously deprives the host galaxy of raw material from which to form new stars (Springel et al. 2005b; Bower et al. 2006; Croton et al. 2006) and starves the black hole, truncating its growth (Silk & Rees 1998; Fabian 1999).

Despite the considerable utility of AGN feedback, there is scant observational data to inform us about how or even if AGN feedback operates in actual galaxies. Arguably some of the most promising cases are instances of mechanical feedback, such as the outflows that have been detected as blue-shifted UV and X-ray intrinsic absorbers in $\sim 50\%$ of Seyfert 1 galaxies and quasars (Crenshaw et al. 1999, 2003; Dai et al. 2008). While it is clear that nuclear outflows are common, it is still difficult to determine the mechanical luminosity (critical for determining if the outflow can unbind circumnuclear gas) and mass outflow rate to determine their impact. A good example of this difficulty is the work of Krongold et al. (2007) on the time evolution of the ionization state of the X-ray absorbers relative to the X-ray continuum in the warm absorber of NGC 4051. From the absorption line variability they obtained good constraints on the density and location of the absorbers from the black hole. Assuming a biconical geometry, they measured a low outflow velocity with respect to the escape speed from the black hole, and a corresponding low mass outflow rate with respect to the accretion rate of the black hole. From these values, they conclude that while the outflows might disrupt the hot ISM, they are not capable of ejecting large amounts of interstellar gas from the host. Whittle et al. (2002, 2005, 2009) reached a similar conclusion for the nearby Seyfert galaxy Markarian 78 using visible-wavelength and radio data to measure the kinematics and ionization state of extended emission-line regions surrounding the active nucleus. They concluded that the biconical outflow in Mrk 78 is weak, slow and heavy, and hence insufficiently energetic to significantly heat or unbind surrounding host galaxy gas.

The results for these two galaxies present an apparent problem for AGN feedback: in both cases the measured AGN outflows are too weak to thermally or mechanically disrupt star formation in the host galaxy. Nevertheless, these are just two objects, and analyses of other AGNs are critical for further understanding the role of AGN feedback in galaxy evolution. Seyfert galaxies are of special interest for detailed studies of AGN feedback as many are luminous enough to be accreting near their maximal Eddington rate, yet close enough to study at relatively high angular resolution (scales of 10–100 pc for nearby examples) using the *Hubble Space Telescope* and ground-based adaptive optics.

A very promising candidate for detailed study is the nearby Seyfert galaxy Markarian 573, which is well-known for its extended, richly structured circumnuclear emission-line regions. Mrk 573 features a prominent ionization bicone and bright arcs and knots of emission-line gas (Ferruit et al. 1999; Quillen et al. 1999) that are strongly aligned and interacting with a kiloparsec-scale low-power radio outflow (Pogge & de Robertis 1993; Falcke et al. 1998; Ferruit et al. 1999). The association between the radio lobes and the emission regions was studied in detail by Falcke et al. (1998), who proposed that the arcs result from gas cooling after passing through a radio-induced radiative bow shock. In contrast, Quillen et al. (1999) argued that the arcs are instead a morphological artifact of dust lanes in the galaxy being illuminated by the nuclear ionizing continuum. This is supported by visible and near-infrared *HST* images that show the emission-line arcs as extensions of larger circumnuclear dust lanes that are illuminated when they pass into the ionization cone. Circumnuclear dust lanes like these are commonly found in active and inactive galaxies alike (Martini et al. 2003), and in the specific case of Mrk 573 they appear to be shaped by the presence of a nuclear bar (Martini et al. 2001), not unlike what is seen in galaxies with inner bars regardless of the presence of nuclear activity.

Ferruit et al. (1999) examined several possibilities for the origin of the arcs and extended emission-line regions using a combination of *HST* images and ground-based, integral-field spectroscopy. They modeled the excitation in the arcs as either shock features, linked to radio jets, or pre-existing structures photoionized by the nucleus. Using standard emission-line diagnostics, they showed that the inner arcs are excited by the central continuum source rather than by fast, photoionizing shocks, citing as evidence that they detected no signs of a strong kinematic interaction through a radio-induced shock. The excitation of the outer arcs was not completely explained by nuclear photoionization; these arcs require an external source of photons in addition to the nucleus to account for the excitation levels. However, their analysis suggested that both the inner and outer arcs show little evidence that they are shock excited.

In this paper we present new long-slit spectrophotometry of Mrk 573 obtained with the Hubble Space Telescope Imaging Spectrograph (STIS). The high angular resolution of STIS, combined with good velocity resolution in the bright $H\alpha + [N II]$ emission lines allows us to examine the excitation and kinematics in these regions in greater detail than possible in previous studies. Our analysis of Mrk 573 follows a threefold approach. First, we examine the kinematics of the circumnuclear emission-line regions to separate kinematically-disturbed gas from quiescent gas in the rotating disk of the galaxy (see sec. 3.1). The existence of these two kinematical components was clear from the

earlier ground-based work, but the greater angular resolution provided by *Hubble* lets us pinpoint the regions of disturbed and undisturbed gas on a scale of 10s of parsecs. Next we measure the densities and temperatures in the emission-line regions using standard nebular diagnostic emission lines. We examine the excitation state of these regions, comparing them with the predictions of published photoionization and shock excitation models to clarify the nature of the ionization mechanism in the bright emission line areas (see sec.3.2). Finally, we undertake a quantitative analysis of the outflow energetics of Mrk 573 using techniques developed by Whittle et al. (2009) to examine the degree of feedback on the host galaxy surroundings (see sec. 4). Throughout this paper we adopt a distance of 74 Mpc for Mrk 573 ($v_{helio} = 5150 \pm 11 \text{ km s}^{-1}$, $H_0 = 70 \text{ km s}^{-1} \text{ Mpc}^{-1}$), giving us a projected linear scale of $\sim 360 \text{ pc arcsec}^{-1}$. For reference, this is approximately half the distance of Mrk 78 ($v_{helio} = 11137 \text{ km s}^{-1}$).

2. Observations and Data Reduction

2.1. Hubble Space Telescope Observations

We acquired spectra of the nucleus of Mrk 573 on UTC 2001 October 17 using the *Hubble Space Telescope* and STIS, with the 52×0.2 aperture. Our data were obtained in one observation period lasting two orbits with two spectral settings: the medium-dispersion G750M grating centered on the $\text{H}\alpha$ emission line, ranging from $\lambda\lambda 6300 - 6850 \text{ \AA}$ and the low-dispersion G430L grating providing coverage from $\lambda\lambda 2900 - 5700 \text{ \AA}$. These configurations provide FWHM spectral resolutions for extended sources of 2.2 and 10.9 \AA respectively, and angular resolution of $0''.051 \text{ pixel}^{-1}$. The spacecraft roll angle was unconstrained in our observation planning as the data were acquired as part of a program to observe the nucleus proper, and an attempt to constrain the slit position angle to the apparent jet axis resulted in plan windows too short for practical scheduling. By pure good fortune, the slit position angle was -70.78° , which is within 16° of the radio-axis position angle of -54° but still passes through the bright part of the inner arcs, well within the ionization cone and the main region of the nuclear outflow seen by others. Figure 1 shows the location of the slit relative to the emission-line regions on a contrast-enhanced “structure map” created from an *HST* F606W image (see Pogge & Martini 2002).

The G750M spectra were acquired as a sequence of three exposures with target exposure times of 1080, 1080, and 840s. The G430L observations consisted of two exposures of 805 and 840s duration. To avoid problems with hot pixels on the STIS CCD, the observations were dithered by $\pm 0''.25$ (5 pixels) along the slit relative to the first spectrum. Wavelength calibration lamp spectra were taken during Earth occultation.

2.2. Data Reduction

Our data were acquired after the primary (Side-1) STIS electronics failed on UTC 2001 May 16. Since the Side-2 electronics did not provide closed-loop temperature control of the STIS CCD, the CCD temperature varies with the ambient temperature of the spacecraft when the thermoelectric cooler is run at a constant rate (Kim Quijano et al. 2003). The result is that the dark rate varies with temperature, and the standard dark calibration images used by the `calstis` data reduction pipeline are often a poor match to the actual dark rates in the hot pixels. To correct for this, we broke out of the `calstis` pipeline after the `BASIC2D` step and corrected the dark pixels individually before re-inserting them into the pipeline for the final wavelength calibration, flux calibration, and geometric rectification steps. In brief, a custom program scanned the Data Quality Frame (DQF) for each individual image and created a list of hot pixels. This list was used to fix all pixels in the science frame that had either negative data values or that deviated from the median within a 7×1 -pixel box centered on that pixel by more than 2σ . For this last step, the long-axis of the analysis box is oriented along the dispersion axis of the detector. Once this hot-pixel surgery was completed for the three G750M observations, the second and third images in the set were then aligned with the first and co-added using the `calstis ocrreject` task to detect and remove cosmic rays. Remaining cosmic rays missed by this step were removed by hand using the median filter routine `TVZAP` in `XVista`. The final combined, cleaned, spectral image was then fed back into the `calstis` pipeline to produce the final calibrated long-slit spectrum. An analogous process was used for each of the two G430L spectra to create the final G430L long-slit spectrum, but because only two images were available, more hand cleaning of residual cosmic rays was required. This process yielded superior results by comparison with the default reduction pipeline. An analogous procedure is described in Rice et al. (2006).

An additional consequence of using the STIS Side-2 electronics is that our long-slit spectra are affected by low-amplitude (2–3 ADU peak-to-peak) fixed-pattern noise with a ~ 3 -pixel horizontal scale that takes the form of a regular herring-bone noise pattern when viewed at high contrast. Attempts to remove this component using fast fourier-transform filtering only made things worse. Its primary effect is to increase the effective readout noise of the device by about $1 e^- \text{pix}^{-1}$ for the gain=1 mode of our data. When extracting faint outer regions of the long-slit spectra, we took particular care to be wary of this fixed-pattern component in interpreting our spectra. The final, calibrated long-slit spectra are shown in Figure 2. We have adopted the nomenclature of Ferruit et al. (1999) for the specific emission-line regions we examine below.

2.3. Spectral Extraction and Line Measurements

The extended emission-line region of Mrk 573 consists of a series of arcs and knots located northwest and southeast of the nucleus along the general direction of the radio outflow. Our STIS slit intersects the arcs but just misses a group of bright knots located along the main radio axis

as shown in Figure 1). We shall focus our attention on four specific regions: the SE1 arc, SE2 arc, the nucleus, and the NW1 arc (Ferruit et al. 1999). The arcs at regions SE1 and NW1 are located at a projected angular distance of $\sim 2''$ on either side of the nucleus, and the SE2 arc is $\sim 3''$ from the nucleus. There is another arc in the Northwest region that is roughly symmetric with the SE2 arc, but the emission lines from this region are too faint and diffuse for detailed analysis with our spectra.

We extracted two 1D spectral data sets from the 2D spectra. The first set is integrated spectra of specific regions of interest for measuring the density, temperature, and excitation state of the line-emitting gas. For these we first created slit intensity profiles for the $\text{H}\alpha + [\text{N II}]$ emission lines in the G750M spectrum and for $[\text{O III}] \lambda 5007\text{\AA}$ in the G430L spectrum, and for adjacent line-free continuum regions bracketing these lines. The derived mean continuum profiles were then subtracted from the line profiles to produce pure emission-line profiles for each line. These profiles were then used in conjunction with the 2D spectra of the nuclear regions (see Figure 2) to precisely locate the windows for extracting 1D spectra of the regions we wished to examine.

The second set of spectra were extracted from the G750M data for making kinematic measurements - line centroids and velocity widths - using the $\text{H}\alpha$ and $[\text{N II}]$ emission lines. For these we extracted 1D spectra in contiguous increments along the slit moving radially outwards from the nucleus. In bright regions we extracted spectra from single-pixel apertures ($0''.2 \times 0''.05$), and as the regions became fainter at larger radii, we increased the width of the extraction window up to a limit of 4 pixels wide ($0''.2 \times 0''.2$) to improve the signal-to-noise ratio in the lines. This gives us nearly continuous spatial sampling along the slit for measuring line-of-sight velocities and emission-line velocity dispersions.

After identifying individual emission lines, we measured the line parameters with the LINER interactive line analysis program developed at Ohio State. For each spectral line, we define a local continuum by averaging over adjacent line-free regions and then fit the lines with a single- or multi-component Gaussian to resolve blends or multiple velocity components if present. We derive the line centroid, Full-Width at Half Maximum (FWHM), and integrated line intensity for each emission-line component present. When fitting doublet lines of a single ionic species (e.g., $[\text{N II}] \lambda\lambda 6548, 83\text{\AA}$ and $[\text{S II}] \lambda\lambda 6716, 31\text{\AA}$) we fit both lines together, imposing physically-motivated constraints on the profile parameters to improve the fidelity of the fits. For the $[\text{S II}]$ doublet, we constrain the relative line centroids in velocity space and match them in line width, but leave the relative intensities (which are correlated with density) unconstrained. For the $[\text{N II}]$ doublet lines, which arise out of the same upper excited level, we constrain their relative line centroids and widths and further constrain their relative line strengths as dictated by the ratio of their radiative transition probabilities. This greatly improves the quality of the fits when deblending these lines from the $\text{H}\alpha$ emission line that lies between them. Some of the emission lines appear double-peaked, particularly in the kinematic spectral extractions. In these cases we model the two peaks as Gaussians and apply similar rules for setting constraints on the physically related line pairs. Finally, if the line of interest is very faint but clearly detectable and unblended, we extract the line

intensity by direct integration without attempting to fit a line profile. The RMS uncertainty in the continuum fits and a simple model for the pixel-to-pixel signal to noise ratio is used to estimate the overall quality of the fit and the uncertainties on the best-fit line parameters.

We make additional checks of our fit-derived line parameters in a number of ways. The total line intensities are compared to a numerical integration of the blend itself without fitting to a particular line shape. Line FWHMs from the fits are compared to direct measurements of the FWHM using profile tracing algorithms that assume no underlying profile shape (this works best for the brightest emission lines with the least blending and highest signal-to-noise ratio). Finally, the Gaussian fit derived line centroids for well-isolated lines are compared to intensity-weighted centroids derived from the central 5 pixels about the peak. All of these give us further estimates of the relative uncertainties, and help alert us to possible systematics that would be missed by simply examining the RMS residuals.

The measured fluxes for various emission lines are listed in Table 1. In general, line centroids and FWHM are measured to $\pm 0.1\text{\AA}$ or $\sim 20\text{ km s}^{-1}$ for the $\text{H}\alpha$ and $[\text{N II}]$ emission lines, with some degradation in fainter regions. Measurement uncertainties for total line fluxes are typically $\pm 10\%$ in the brighter lines, increasing to $\pm 20\%$ in the faintest regions measured.

3. Spectral Analysis

We pursue two different analyses of our spectra. The first uses the kinematic spectra (sec. 3.1) to derive outflow speeds and separate outflowing gas from ambient ISM gas in orderly rotation in the disk. Combining the outflow kinematics with the emission-line geometry seen in the direct images provides us with constraints on the configuration of the outflow, allowing us to deproject the observed radial velocities and thus determine the actual physical outflow velocities.

The second line of analysis uses emission line diagnostics from the spectrophotometric set of spectra (sec. 3.2) to estimate the density, temperature, and excitation state of the gas in these regions. These are compared to published models of shock- and photo-ionized gas to determine the excitation mechanism in these regions.

3.1. Emission Line Kinematics

Figures 3 and 4 show the radial velocities along our long slit for the $\text{H}\alpha$ $\lambda 6563\text{\AA}$ and $[\text{O III}]$ $\lambda 5007\text{\AA}$ emission lines¹. A number of distinct kinematic systems are present. The largest-scale pattern is a rotating disk extending out as far as we can trace ionized gas (roughly $\pm 4''$), with the

¹Radial velocity measurements for $\text{H}\beta$ $\lambda 4861$, $[\text{N II}]$ $\lambda\lambda 6548, 6583$, and $[\text{O III}]$ $\lambda\lambda 4363, 4959\text{\AA}$ lines show consistent results and are available upon request.

NW side receding and the SE side approaching us and an amplitude of roughly $\pm 125 \text{ km s}^{-1}$. In the inner $1''$ on either side of the nucleus the kinematics are dominated by a coherent system of double-valued radial velocities (separated by nearly 300 km s^{-1}) with a red/blue splitting pattern characteristic of a biconical outflow (e.g. Crenshaw et al. 2000; Das et al. 2005). Finally, in the inner $0.5''$ around the nucleus we see various additional $\text{H}\alpha$ velocity components with no obvious pattern associated with the inner parts of the outflow region. The high-velocity components of the biconical outflow pattern and the large-scale rotation pattern are also visible in the $[\text{O III}] \lambda 5007 \text{ \AA}$ line-of-sight velocities (Figure 4) despite the lower dispersion of the G430L grating.

In the biconical outflow models of Crenshaw et al. (2000) and Das et al. (2005) emission from the front of the cone (the surface closest to the observer) is blueshifted and the back of the cone is redshifted. When the bicone axis is at high inclination angles (the cone axis near the line of sight) there is a strong blue-to-red asymmetry in the radial velocities, while at low inclinations (the axis near the sky plane), the radial velocity pattern is more symmetric (Das et al. 2005). In the context of these models, our radial velocity maps indicate that the biconical outflow in Mrk 573 has a relatively low inclination with the NW cone directed toward us. Using the velocities from our $\text{H}\alpha$ emission line, the observed ionization cone opening angle of $\theta_C = 45^\circ \pm 10$ (Wilson & Tsvetanov 1994), and assuming a constant velocity, v_f , of material in a shell along the cone and a slit roughly aligned with the cone axis, the Das et al. (2005) outflow model gives projected velocities of

$$v_{Red} = v_f \sin(\theta_C + \phi) \approx 200 \text{ km/s} \quad (1)$$

$$v_{Blue} = v_f \sin(\theta_C - \phi) \approx 100 \text{ km/s} \quad (2)$$

for the red and blue sides of the cone, respectively. The cone opening angle (θ_C) is related to these velocities and the cone inclination angle (ϕ) by

$$\tan(\theta_C) = \left(\frac{v_{Red} + v_{Blue}}{v_{Red} - v_{Blue}} \right) \tan(\phi) \approx 3 \tan(\phi) \quad (3)$$

which gives a bicone inclination angle of $\phi = 18^\circ \pm 4^\circ$ and $v_f = 220 \text{ km s}^{-1}$ for the nuclear outflow in Mrk 573. We model this outflow geometry in Figure 5.

Between about $1-1.5''$ from the nucleus there is very little emission line gas, and so we have no measurements in these regions. This region between the nucleus and the two close emitting arcs likely represents the nearly evacuated “bubbles” resulting from the biconical outflow. Beyond about $1.5''$ on either side of the nucleus a coherent pattern of velocities consistent with a rotating disk of relatively undisturbed gas extends out to the limits of our long-slit data. This sense of rotation (SE approaching, NW receding) is opposite the direction of the biconical outflow which helps to distinguish these components. At the location of the bright arcs (SE1 and NW1), the kinematics are disturbed: the radial velocities split by $\sim 100 \text{ km s}^{-1}$ relative to the rotating disk pattern, and the velocity dispersion jumps dramatically in the SE1 arc to nearly 300 km s^{-1} . This can be seen in the 1D radial velocity profile (Figure 3, middle panel) and in the 2D spectrum (Figure 2) where the $\text{H}\alpha$, $[\text{N II}]$ and $[\text{S II}]$ emission lines are all suddenly broader. The effect is less obvious in the

fainter NW1 arc, although in the 2D spectrum there is faint but noticeable broadening of the $H\alpha$ and $[\text{N II}]\lambda 6583\text{\AA}$ lines. These are the regions that Ferruit et al. (1999) identified with the working surface between the radio outflow and ambient gas in the galaxy. The SE2 arc appears to have similar kinematic disturbance as SE1 and NW1 in the $[\text{O III}]$ velocity map; however, it is not consistently double-valued in $H\alpha$, like the other two arcs (see Figure 3, 4). This implies that SE2 is not significantly kinematically disturbed as SE1 and NW1 are. Throughout this analysis, we include calculations for SE2, but our primary focus is on the effect of an outflow as manifested in SE1 and NW1.

3.2. Spectrophotometry

The spectra of the nucleus and bright, off-nuclear regions are remarkably rich in emission lines, as can be seen in Figure 6 where we plot the spectra of the nucleus and the brightest off-nuclear regions. Of particular interest are the lines of $H\alpha$, $H\beta$, $[\text{N II}]\lambda\lambda 6548, 6583\text{\AA}$, $[\text{O III}]\lambda\lambda 4363, 4959, 5007\text{\AA}$, and $[\text{S II}]\lambda\lambda 6716, 31\text{\AA}$ which are used to estimate internal extinction, densities, and temperatures in the gas, and provide diagnostics of shock versus photoionization. In addition, we can observe a number of fainter high-excitation lines of interest, including $[\text{Fe X}]\lambda 6375\text{\AA}$ and the $[\text{Ne V}]\lambda 3426\text{\AA}$ line.

3.2.1. Densities and Temperatures

The densities of the emission-line gas are estimated using the $[\text{S II}]\lambda\lambda 6716, 31\text{\AA}$ doublet ratio and the theoretical calculations of Cai & Pradhan (1993). The gas temperatures are calculated using the $[\text{O III}]\lambda\lambda 4363, 4959$, and 5007\AA emission lines following the method described by Osterbrock (1989). Because the $[\text{O III}]$ emission-line ratio $I(4959) + I(5007)/I(4363)$ is reddening-sensitive, we estimate the effects of extinction by assuming a simple screen geometry and using the H I Balmer decrement assuming Case-B recombination. The small differences between the observed and emitted $[\text{O III}]$ line ratios in Table 2 indicate that reddening in these regions is negligible.

Because the $[\text{S II}]$ doublet density method is weakly temperature dependent and the $[\text{O III}]$ temperature estimate is weakly density dependent (see Osterbrock 1989), we have adopted an iterative approach, whereby we first estimate the $[\text{O III}]$ temperature in the low-density limit, evaluate the $[\text{S II}]$ density at that temperature, and then use that density to re-evaluate the $[\text{O III}]$ temperature, iterating until the solutions converge to within the measurement uncertainties. The densities we find range from $760\text{--}2500\text{ cm}^{-3}$, and the temperatures range between $10000\text{--}14500\text{ K}$. The resulting temperature and density estimates for each region and their uncertainties are given in Table 2.

3.2.2. Emission Measures

The arcs are high-surface brightness emission-line features, but the “bubbles” between SE 1, NW 1, and the nucleus (B_{SE} and B_{NW} respectively) are very low surface brightness. As the bubbles have only very weak emission lines, we cannot estimate the temperature and density using standard metal-line diagnostics. Instead, we make an order-of-magnitude estimate of the mean density $\langle n_e \rangle$ using the emission measure (EM) derived from the surface brightness of $H\beta$ ($I(H\beta)$), an estimate of the line-of-sight thickness of the bubbles, D , and the volume filling factor f :

$$EM = \frac{4\pi I(H\beta)}{h\nu_{H\beta}\alpha_{H\beta}^{eff}(T)} = \int_{los} n_e n_p ds \approx \langle n_e^2 \rangle Df \quad (4)$$

We assume that the temperature is roughly constant, and that the bubbles are roughly spherical (i.e., as thick as they are wide) and have unit filling factor. A first estimate assumes a temperature of 15000 K, slightly higher than the temperature of the nuclear region, to evaluate the effective recombination coefficient, giving a mean density of $\sim 1 \text{ cm}^{-3}$ in the bubbles (see Table 3). At this temperature and density the gas in the bubbles is out of thermal pressure balance with the gas in the emission-line arcs just outside them by a factor of ~ 500 -1500. The bubbles may instead be more like supernova bubbles with internal temperatures of $\sim 10^6$ K; adopting $T = 10^6$ K gives emission-measure derived mean densities an order of magnitude larger (see Table 3), bringing the bubbles into rough thermal pressure balance. The latter temperature is consistent with thermalization of bulk motions with velocities as observed, i.e. $\sim 200 - 300 \text{ km s}^{-1}$.

3.2.3. Nuclear Emission

While the bubble regions have only very weak emission lines, the nuclear emission spectrum has many high ionization lines that are undetected in other emission-line regions, notably [Fe X] $\lambda 6375\text{\AA}$, [Ar V] $\lambda 6435\text{\AA}$, and [Ar IV] $\lambda\lambda 4711, 4740\text{\AA}$ (see Figure 6). The presence of these lines indicates that the photons emitted from the nucleus have a sufficiently hard spectrum to substantially ionize the surrounding material. Some of these lines appear to be double peaked; in particular [Fe X] $\lambda 6375\text{\AA}$ has a broad, flat top. This feature is best fit by two blended Gaussian lines, at $\lambda 6483$ and $\lambda 6486\text{\AA}$, respectively, corresponding to line-of-sight velocities of -46 and $+92 \text{ km s}^{-1}$. This line splitting likely represents highly excited gas at the base of the biconical outflow.

3.2.4. Emission Line Diagnostics

Shock-ionized gas will have different relative emission line strengths than gas photoionized by the active nucleus. Collisionally excited UV resonance lines provide the best discriminants between shock and photoionization due to the higher temperatures expected in the shocked gas (Dopita 2002; Allen et al. 1998). Unfortunately, we do not have near-UV spectra of Mrk 573 and therefore

we must use visible-wavelength indicators.

To evaluate the importance of shock excitation for the arcs, we compare the fluxes of our observed optical emission lines (Table 1) to the predictions from models for ionizing shocks with precursors, photons traveling ahead of the shock front, and nuclear photoionization calculated by Whittle et al. (2005) and Allen et al. (2008). The shock models cover a range of shock speeds ($v_s = 200 - 1000 \text{ km s}^{-1}$) and magnetic field strengths, $B/\sqrt{n} = 0 - 10 \mu\text{G cm}^{3/2}$. We adopt two illustrative photoionization models from Whittle et al. (2005). The first is a power-law photoionization model for optically thick gas with a density of 10^2 cm^{-3} and a nuclear continuum with a spectral index of $\alpha = 1.4$ (where $f_\nu \propto \nu^{-\alpha}$). This model covers photon energies from 50 keV to 100 μm with an ionization parameter range of $\log U = -4.0$ to 0.5. The second is the “ U_{dust} ” model that is similar to the first but includes a realistic dust component that accommodates changes in the internal structure of dusty clouds in response to the incident radiation field from Groves et al. (2004). This second model is for a density of 10^3 cm^{-3} , continuum spectral index of $\alpha = 1.4$, and a metallicity twice the solar abundance.

Figure 7 shows four emission-line diagnostic diagrams that provide the cleanest discrimination between shock and central photoionization for the lines available in our spectra. The upper two panels show two diagnostics using the [O I] $\lambda 6300\text{\AA}$ line: [O III]/H β vs. [O III]/[O I] and [O III]/H β vs. [O I]/H α . In both cases the data are in best agreement with the simple, $U_{1.4}$ photoionization model and appear to disfavor the shock sequences and to a lesser extent the U_{dust} model. However, these results should be viewed with some caution as the [O I] line is difficult to model: in photoionization models the [O I] is formed in a partially ionized zone heated by X-ray photons, while shock models are known to overpredict the [O I] line strength by as much as an order of magnitude (e.g. Groves et al. 2004).

The lower left panel of Figure 7 shows the [O III]/H β vs. [S II]/H α diagnostic in which the photoionization and shock models are essentially orthogonal to one another. Here the nucleus and SE2 region are in better agreement with the photoionization model, while the NW1 and SE1 arc regions are ambiguous between photoionization and a relatively fast shock ($v > 500 \text{ km s}^{-1}$) with a strong magnetic field ($B/\sqrt{n} = 10 \mu\text{G cm}^{3/2}$), while they are in good agreement with the U_{dust} model. In the last panel we show the [Ne V]/[Ne III] vs. [Ne III]/[O II] diagnostic. These line ratio measurements are similar to the previous panel, in particular the agreement between the NW1 and SE1 measurements and the shock models, while the nucleus and SE2 region do not agree well with any of the models. One caveat with this diagram is that [Ne III] may be overpredicted by the models (Whittle et al. 2005).

While none of these line ratios are ideal discriminants between shock and photoionization, we nevertheless see consistent trends in our analysis that favor photoionization. One interesting aspect of these data is that the SE1 and NW1 arc regions, which trace the most morphologically-obvious bowshock structures, are more consistent with shock models than either the nucleus or the SE2 region. This also supports our assertion that SE2 is not strongly interacting with a biconical

outflow. Additional far UV data could prove useful to further investigate the strengths of any shocks in these regions; however, based on these and previous arguments we conclude that the emission line ratios in all four regions are more consistent with photoionization than with shocks. While they themselves are not a clear cut indicator of photoionization, they do support the findings from kinematics and analysis of energetics.

3.3. Discussion: Ionization Mechanisms

Our analysis thus far adds additional detail to the picture for the inner regions of Mrk 573 developed by previous work: a hot biconical outflow emerging from the nucleus that is running into the host galaxy at the location of the bright emission-line arcs. Our kinematic data show that this outflow is mildly inclined with respect to the host galaxy disk ($18 \pm 4^\circ$), and there is a modest kinematic disturbance at the location of the arcs. The inner part of the outflow between the dense base of the bicone and the arcs has low density ($\sim 1 \text{ cm}^{-3}$)

The nature of the arcs from previous work has been equivocal. On the one hand, Ferruit et al. (1999) inconclusively modeled these same emission regions as either pre-existing structures or shock features, while on the other *HST* images show dust lanes that extend beyond the ionization cones which led Quillen et al. (1999) to suggest that the arcs of Mrk 573 do not result from bow shocks. Our analysis of the densities of the different emission line regions reveal that the arcs and nucleus have similar densities, implying that the arcs were not formed by a fast shock. A fast shock would have slammed into the surrounding material, making it more dense, which we do not observe. The density values support the morphological argument of Quillen et al. (1999) that the central photons are ionizing pre-existing dust lanes. In turn, this supports the suggestion of Ferruit et al. (1999) that any shock from the central AGN is too weak and slow to photoionize the surrounding material.

Analysis of the evacuated regions, the bubbles, compared to the emission line regions also supports central photoionization of dust lanes. If these bubbles were rapidly expanding and compressing the surrounding material, they would shock ionize the arcs. In this scenario we expect a higher pressure inside the bubbles than the arcs to cause the expansion. Our calculation of the emission measures (see sec. 3.2.2) reveals that the bubbles have ~ 500 - 1500 times less thermal pressure than the arcs, assuming a temperature of 15000 K . When we assume a temperature of 10^6 K , motivated by plausible shock velocities, the thermal pressure in these regions is still only ≈ 0.1 - 1 times the amount in the emission line regions (see Table 3). For the bubbles to be rapidly expanding into the surrounding material, bulldozing it, they need to have higher pressure than their surroundings. Over a large range of temperatures, the pressure in the bubbles is simply not large enough for the amount of expansion that would result in arc creation and shock ionization.

4. Properties of the Nuclear Outflow

Our spectrophotometric analysis of Mrk 573 indicates that the emission line regions are likely photoionized by the nuclear source. If there is a shock present, it is not strong enough to form the material into arcs and ionize it, agreeing with the conclusion of Ferruit et al. (1999). We now complement these analyses with a detailed investigation of the emission-line region and outflow energetics, quantifying the outflow’s interaction with the host galaxy ISM. Specifically, we estimate the energies and pressures of the emission-line regions (section 4.1) and relate them to values calculated for the outflow (section 4.2). These analyses broadly follow the techniques applied by the Whittle et al. (2009) study of Mrk 78, and we shall adopt similar notation. By comparing the values of the different energy components of the outflow and emission line regions, we can confirm that the emission line regions are photoionized. The various energies also indicate the importance of mechanical feedback, and the overall strength of the outflow present (section 4.3). We also compare our results to those of the analogous emission-line regions studied by Whittle et al. (2009), and demonstrate that Mrk 573’s emission-line regions are very similar to what is observed in Mrk 78.

4.1. Emission Regions: Masses, Energies and Pressures

To understand the relationship between ionized and neutral gas in the emission regions, we estimate the values of the various energy components. This is critical for determining what contributes to the kinematics, ionization, and structure, in addition to the relative importance of mechanical feedback on the host. We are able to calculate the energy of the various components by building off of determinations of the flux, mass and lifetimes of the emission line regions.

We assume that the portion of a given emission-line region within the slit is representative of the larger region as a whole, and so multiply the flux within the slit by the ratio of the total region area ($\theta_{ex} \times \theta_{ey}$) to the slit region area to approximate the total flux. The slit regions are the width of the slit, $0.2''$ multiplied by the size in arcseconds each region covers in the pure emission-line profiles (see sec. 2.3, Table 1). The physical sizes of the regions that we use are listed in Table 4. Our region sizes and fluxes are smaller than those measured by Ferruit et al. (1999) because we can better distinguish the sharp boundaries with our improved resolution; Ferruit et al. (1999) had an angular resolution of $\approx 0''.35$ FWHM compared to our STIS resolution of $0''.1$ FWHM.

The ionized gas mass in each emission-line region (M_{em}) may be estimated from the $H\beta$ emission-line luminosity and the electron density n_e derived from the [S II] doublet ratio from recombination theory:

$$M_{em} \approx \frac{L_{H\beta} m_p}{h\nu_{H\beta} n_e \alpha_{H\beta}} \approx 8 \times 10^{14} \left(\frac{cz}{H_0}\right)^2 F_{H\beta}(n_{em,3})^{-1} M_{\odot} \quad (5)$$

In this and subsequent equations, the numerical subscript appended to a variable indicates a logarithmic scaling, e.g. $n_{em,3}$ represents density in units of 10^3 cm^{-3} . The interaction age of the

region, t_{em} , is estimated as the crossing time, t_{cross} , the amount of time required for a compact parcel of gas expanding outwards at V_{em} to traverse the distance from the nucleus to the arcs, i.e.

$$t_{em} \approx t_{cross} \approx 47100 \left(\frac{cz}{H_o} \right) \theta_{ex} (V_{em,2})^{-1} \tan \phi \text{ yr} \quad (6)$$

where θ_{ex} is the angular separation between the nucleus and arcs in units of arcseconds. The emission-line masses for NW1 and SE2 are both $\sim 10000 \pm 2200 M_\odot$, while SE1 is less massive, $\sim 7000 \pm 1500 M_\odot$. SE1 has an interaction age of 3.53 ± 1.3 Myr, and NW1 is 2.24 ± 0.7 Myr old. SE2 has the largest interaction age, $t_{em} \approx 6.90 \pm 2.5$ Myr. This is the expected age progression, in that SE2 lies further from the nucleus than SE1 and NW1. However, we must note that SE2 does not appear to be strongly interacting with the biconical outflow, based on its lack of kinematic disturbance in $H\alpha$ (see Figure 3). We use the interaction age of SE2 to determine other properties of the emission-line region to better understand the basic energetics of the region, but it is merely an approximation. The age determinations for all of the regions are consistent with what is seen in Mrk 78 by Whittle et al. (2009) from emission-line structures of comparable scale (0.4–8.2 Myr).

The total energy in the emission-line regions, E_{em} , may be estimated from the product of the interaction age and the luminosity in the $[O \text{ III}]\lambda 5007\text{\AA}$ emission line which measures the nebular cooling power:

$$E_{em} = 1.2 \times 10^{51} \left(\frac{cz}{H_o} \right)^2 F_{5007} \times t_{em} \quad (7)$$

where F_{5007} is the $[O \text{ III}]$ line flux in cgs units. Each of the regions has total emission energy on the order of 10^{55} ergs.

There are three energy components of interest in the emission line regions associated with their mechanical and thermal energy content. The translational kinetic energy, $E_{kin,t}$, of the outflowing gas may be estimated from the mass of the region and its transverse velocity, V_{em} ,

$$E_{kin,t} \approx \frac{1}{2} M_{em} V_{em}^2 \text{cosec}^2 \phi \approx 10^{53} M_{em,6} (V_{em,2})^2 \text{cosec}^2 \phi \quad (8)$$

where we use the estimated bicone inclination angle ϕ to deproject the observed radial velocity. The internal (turbulent) kinetic energy, $E_{kin,i}$, depends on the emission-line mass and velocity full-width, W_{em} :

$$E_{kin,i} \approx \frac{1}{2} M_{em} (W_{em}/2.35)^2 \approx 1.8 \times 10^{52} M_{em,6} (W_{em,2})^2 \quad (9)$$

Whittle et al. (2009) used the width of the $[O \text{ III}]\lambda 5007\text{\AA}$ emission line, but because we have only low-dispersion spectra in which these lines are either unresolved or marginally resolved at their broadest, we instead use the widths of the $H\alpha$ and $[N \text{ II}]$ emission lines. Finally the thermal energy, E_{th} , is

$$E_{th} \approx \frac{3}{2} NkT \approx 4.1 \times 10^{51} M_{em,6} T_{e,4} \quad (10)$$

where we use the electron temperatures derived from the $[O \text{ III}]$ emission lines. All of these energies are listed in Table 4. In general, the translational kinetic energy in the regions is about 100 times

larger than the thermal energy. This is consistent with our earlier suggestion that the gas is not significantly shocked, or if shocked it has had enough time to cool to the $\sim 10^4$ K temperatures observed. This implies that the acceleration mechanism must be fairly slow and gentle (the typical gas speeds are $\sim 100 - 200 \text{ km s}^{-1}$ in these regions, about an order of magnitude larger than the sound speed for 10^4 K gas). The internal kinetic energy is roughly 10 times larger than the thermal energy, suggesting that this motion is not supersonic turbulence but instead is bulk motion of the gas along the line of sight that is unresolved at our scales, for example an expansion of order $\pm 100 \text{ km s}^{-1}$ along the line of sight at the point of contact between the nuclear outflow and the emission-line gas in the SE1 and NW1 arcs.

Our spectrophotometric analysis of Mrk 573 suggests that the emission-line regions are photoionized by the active nucleus rather than ionized by fast shocks. We investigate two sources of energy input into these regions. The first is the available photon energy, E_{ph} , from the active nucleus. We use the IRAS $60 \mu\text{m}$ and $100 \mu\text{m}$ flux from Mrk 573 to estimate the nuclear bolometric luminosity by assuming that all photons from the central source are absorbed and re-emitted in the infrared by surrounding dust, which underestimates the actual luminosity. Each region's E_{ph} follows from the fraction of nuclear energy that is intercepted by the arc, the covering fraction cf , over its interaction age (t_{em}) assuming that the regions have unity filling factor

$$E_{ph} = 1.5 \times 10^{39} \left(\frac{cz}{H_0} \right)^2 [2.6S_{60} + S_{100}] \times t_{em} \times cf \quad (11)$$

For the covering fraction, we assume that the depth of the cloud is approximately the arc thickness, θ_{ey} . The depth could in fact be ~ 10 times this size, increasing the photon energy by this same factor. For our purposes, being conservative with our covering fraction is acceptable, as even with this small value, E_{ph} is significantly larger than all other energy sources in the emission regions.

The second source of energy is relativistic energy, E_{rel} , stored in the radio outflow, which provides an estimate of the energy input due to expansion of the radio lobes into the circumnuclear gas. E_{rel} depends on the minimum magnetic field strength, B_{min} , a lower limit found by assuming equipartition between the relativistic particles and the magnetic field

$$B_{min} \approx 2.93 \times 10^{-4} \left(\frac{S_\nu}{\theta_{rx}\theta_{ry}} \frac{a(1+z)^{3+\alpha_r} \left(\frac{30}{\lambda}\right)^{\alpha_r} X_{0.5}(\alpha_r)}{f_{rel}\theta_{ry}\left(\frac{cz}{H_0}\right)} \right)^{2/7} \quad (12)$$

$$\text{where } X_q = \frac{(\nu_2^{q-\alpha_r} - \nu_1^{q-\alpha_r})}{q - \alpha_r}$$

Where α_r is the radio spectral index, and f_{rel} is the filling factor. The spectral indexes are observed to be $\alpha_r \approx -0.85$ for NW1 and -0.5 for SE1 (Falcke et al. 1998). For the projected size of the radio outflow working surface we adopt θ_{rx} and θ_{ry} to be $\sim 0''.1$. We adopt $a \approx 2$, where a represents the contribution of relativistic energy density by ions in proportion to the contribution by electrons, following Whittle et al. (2009) and assume unity filling factor for the relativistic material ($f_{rel} = 1$). Following our calculation of B_{min} , the available relativistic energy, following Whittle et al. (2009),

is thus

$$E_{rel} \approx 1.6 \times 10^{56} \theta_{rx} \theta_{ry}^2 f_{rel}^{3/7} \left(\frac{cZ}{H_o} \right)^3 B_{min}^2 \quad (13)$$

The estimates for the NW1 and SE1 regions are listed in Table 4.

Our calculations of the energies of the different components in the emission line regions and the potential sources indicates that E_{ph} dominates, being ~ 1000 times larger than E_{rel} and about 10 times larger than the total energy in the emission regions, E_{em} . A complete discussion of the different energy components follows in sec. 4.3.

The energetics of the emission line region and its possible radiative and relativistic sources are important for understanding the host-AGN interaction, and how it manifests itself. Similarly, examination of the different pressures can reveal whether the relativistic pressure from the radio lobe expansion or the radiative pressure from the central photon source are responsible for the arc structures. Following Whittle et al. (2009), we calculate the emission-line region thermal pressure (P_{em}), the relativistic pressure (P_{rel}), and the radiation pressure (P_{rad}), expressed in dynes cm^{-2} :

$$P_{em} \approx 1.4 \times 10^{-9} n_{em,3} T_{em,4} \quad (14)$$

$$P_{rel} \approx 0.031 B_{min}^2 f_{rel}^{-4/7} \quad (15)$$

$$P_{rad} \approx 2.1 \times 10^{-11} [2.6S_{60} + S_{100}] \Delta_e^{-2} \quad (16)$$

where Δ_e is the distance from the region to the active nucleus. The thermal pressure, P_{em} , is based on the temperatures and densities determined from our spectrophotometric analysis. The relativistic pressure, P_{rel} , which results from radio lobe expansion is based on the calculated magnetic field B_{min} . Lastly the radiation pressure from the central photons, P_{rad} , is based on the FIR values, similar to our calculation of E_{ph} . We find $P_{rel}:P_{em} \approx 15:1$, with P_{rad} contributing negligibly. In the next section we describe our methods for quantifying the properties of the outflow itself, rather than its effect on the emitting material. We combine these two analyses in section 4.3, and use the results to determine how much influence the nuclear outflow of Mrk 573 has on its host.

4.2. Effect of an Outflow: Velocities and Dynamical Pressures

Beyond analyzing the energies and pressures of the emission line regions, we can quantify parameters of the outflow itself, in particular the velocity and dynamical pressure. This allows us to determine the outflow's strength directly, rather than conjecturing it based upon the behavior of surrounding material. As the outflow does not appear to be affecting SE2, we only determine properties of it with respect to NW1 and SE1.

The strength of the outflow is dependent upon its composition. A relativistic outflow, in the form of a jet, with speed V_o approximately equal to the speed of light, is able to both bulldoze and shock-ionize material. For an outflow with both thermal and relativistic material, the thermal component literally weighs down the outflow, slowing it down to $\sim 10^3 \text{ km s}^{-1}$ (Whittle et al. 2009).

Thus, outflow speed reflects the amount of thermal and relativistic material present. Whittle et al. (2009) have suggested that the outflow of Mrk 78 is a heavy thermal jet, making it too weak to have significant influence over its surroundings. Through our quantitative analysis of the outflow in Mrk 573, we can determine whether or not it is also heavy and weak.

The approximate speed of the outflow is estimated from the energy and momentum values. An outflow with both material components can contribute to the kinetic and relativistic energy of the emission line regions; it can also affect the momentum of the emitting material, G_{em} . Thus, we use these values to determine V_o , the speed of the outflow. Following Whittle et al. (2009):

$$V_o = 2 \frac{E_{kin} + E_{rel}}{G_{em}} \left(1 + \frac{1}{R_{kin}} \right)^{-1} \quad (17)$$

where R_{kin} is the ratio of kinetic energy to relativistic energy. If we assume the outflow primarily consists of heavy thermal material, making $R_{kin} \sim 1$, we calculate velocities of $\sim 300 - 2000 \text{ km s}^{-1}$ (see Table 4), which is greater than the observed emission-line regions' speeds by factors of $\sim 10-100$. This supports the suggestion that the outflow in Mrk 573 is primarily made up of thermal material. A primarily relativistic outflow would have velocities vastly more than $\sim 10-100$ times the emission-line velocities, and we do not calculate speeds of this extent.

The thermal component of the outflow drives dynamical pressure, $P_{o,dyn}$, into its surroundings. Following Whittle et al. (2009):

$$P_{o,dyn} = \frac{\Pi_o}{A_o} \quad (18)$$

where A_o is the area of the outflow, which we measure from the radio maps of Falcke et al. (1998) to be $\approx 0.60 \text{ arcsecond}^2$, and we assume that Π_o , the force of the outflow, is $\approx \Pi_{em}$, the force in the emission line regions, calculated using the momentum and crossing times. We can then compare the ram pressure of the outflow to the pressures measured for the emission regions and evacuated bubbles, finding that it is significantly less than P_{em} and P_{rel} . Following this, we use the dynamical pressure calculation to determine the Mach number of the outflow.

$$N_{Ma}^2 \approx \frac{3P_{o,dyn}}{5P_{rel}} \quad (19)$$

As listed in Table 4, the estimated Mach numbers, though uncertain, are very small, on the order of 0.01, confirming that the outflow is slow and thus, likely dominated by thermal material, similar to the outflow in Mrk 78 (Whittle et al. 2009).

A final aspect of our outflow analysis is to determine the amount of mass the outflow transports. This value quantifies the influence of the outflow on its surroundings. The mass flux is:

$$\dot{M}_o = \frac{\Pi_o}{V_o} \quad (20)$$

and is $\sim 10^{-11} \text{ M}_\odot \text{ s}^{-1}$ based on our estimates above.

4.3. Discussion: Outflow Strength

Our spectrophotometric analysis suggested that the outflow in Mrk 573 is unable to bulldoze material into the emitting arcs. Through analysis of the physical properties of the emission regions and the outflow, we can confirm this picture.

As shown in section 4.1, the relative proportions of each of the energy components is $E_{ph} : E_{em} : E_{rel} : E_{kin} : E_{th} \approx 10^4 : 3000 : 10 : 1 : 0.01$ (see Table 4), similar to what was found in Mrk 78 by Whittle et al. (2009). The photon energy E_{ph} clearly dominates. The emission-line region energy E_{em} is $\sim 25\%$ of E_{ph} , confirming that central photoionization alone is sufficient to be the ionizing source of the emission regions. The relativistic and kinetic energies, while both substantially smaller than the emission-line region energy, are comparable to each other. This implies that the slow expansion of the radio source into the surrounding material is able to drive the small amount of kinematic activity in the emission-line regions. Also note that SE2, where there is little evidence of interaction between the material and an outflow, has very similar energy magnitudes to SE1 and NW1. Despite the fact that NW1 and SE1 are in the direct path of the outflow, the regions appear quite similar to non-affected material, implying that an outflow has little influence on the emission-line regions' properties.

We further investigate the kinematics by looking at the different pressures in the regions. The radio outflow pressure P_{rel} is slightly larger than the ionized gas pressure, P_{em} , indicating that the small kinematic motions in the emission regions are caused by the gentle expansion due to the radio outflows. Our previous analysis of the densities and temperatures of the emission regions and the evacuated bubbles shows that the bubbles have comparable or less thermal pressure than the arcs over a wide range of temperatures. This supports the conclusion that any expansion of the outflows is gentle. The radiative pressure P_{rad} is markedly less than the emission-line region thermal pressure, and therefore makes no significant contribution to the emission-line region kinematics we observe. We also investigate the dynamic pressure contribution from the thermal component of the outflow, which has been suggested as a potentially significant pressure source (Bicknell et al. 1998). However for Mrk 573 the dynamic pressure is less than the relativistic pressure. The dynamic pressure would have to be significantly larger than the relativistic pressure or comparable to P_{em} to be able to push around the host ISM significantly. In this case, however, it appears that the expansion is caused primarily by the radio lobes, with the mechanical contribution of the outflow being supplementary at best, and likely negligible.

Our calculation of the amount of material transported by the outflow also indicates that it has little influence over the host. The outflow can transport $10^{-4} M_{\odot} \text{ yr}^{-1}$ of material. Over the calculated lifetimes of the outflows, they have carried at most a tenth of the emission mass. Strong jets have been measured carrying as much as $\sim 0.6 M_{\odot} \text{ yr}^{-1}$ (Bicknell et al. 1998), significantly more than we calculate here, once again pointing towards the general impotence of the outflow in Mrk 573.

The energy analysis shows that radio outflow contributes primarily to the kinetic energy of

the ionized region but not to its ionization, while the pressure analysis shows that the outflow does not strongly expand into the surrounding material. While these estimates have significant uncertainties associated with them, the differences between the estimated energies, pressures, etc. are large enough that we can clarify the relationship between the outflow and host despite this uncertainty. Taken together, the data suggest that the host galaxy of Mrk 573 is photoionized rather than shock-ionized, and that the radio outflow gently shapes the regions but does not otherwise contribute to its ionization or heating significantly. This is similar to what Whittle et al. (2009) found for Mrk 78.

The extensive evidence that the emission regions of Mrk 573 are pre-existing structures photoionized by a nuclear source also support that the outflow itself is weak and likely thermal. An outflow made up of primarily thermal material is slower and therefore less able to bulldoze and strongly shock surrounding material. Earlier work by Bicknell et al. (1998) on the outflow in NGC 1068 has found similar results, suggesting that the radio jets in Seyferts differ from those in radio galaxies and quasars primarily in that they are dominated by thermal gas instead of light relativistic material. Our analysis of the outflow speeds confirm that Mrk 573 has a slow outflow, orders of magnitude slower than one dominated by relativistic material. This suggests that the outflow of Mrk 573 is similar to the weak heavy jet that is incapable of shocking material and being the primary ionization mechanism in Mrk 78 (Whittle et al. 2009).

Combining the different facets of this quantitative analysis presents a consistent picture of a slow, heavy outflow capable of gently shaping the surrounding host ISM into the arcs we see, but not fast enough to substantially heat, displace, or ionize that material.

5. Summary

We have examined the influence of the AGN in Mrk 573 on its host galaxy using high angular resolution spectrophotometry from *HST* STIS. These spectra provide both kinematic and spectrophotometric measurements from which we derive the kinematics and physical state of the gas in the circumnuclear regions associated with an interaction between a nuclear radio outflow and spiral dust arms in the host galaxy. Arguments from emission-line diagnostics and thermodynamics (energy and pressure in the various components) lead us to conclude that the outflow from the active nucleus in Markarian 573 does not strongly influence the surrounding ISM other than gently sculpting the material into arcs. The dominant source of the heating and ionization in the gas can be entirely explained by photoionization by energetic photons from the active nucleus proper. This is similar to what has been seen in other, well-studied nearby AGN outflows with sufficient data to make similar energetics arguments, particularly the work of Whittle et al. on Mrk 78. In many ways, Mrk 573 and Mrk 78 are very similar energetically and morphologically: they have hot, heavy outflows sculpting extended emission-line regions lit-up by ionizing photons from the nucleus.

All of the outflow and photoionization energetics taken together suggest that while there is

some feedback on the AGN’s host, it is relatively gentle and insufficient to unbind the host ISM or otherwise shutdown star formation by many orders of magnitude. The outflows expand gently into the host and have transported at most a tenth of the mass in the emission regions over their lifetimes. The star formation regions in the inner few kiloparsecs of Mrk 573, seen as wound spiral arms outlined by H II regions (Pogge & de Robertis 1995), appear to be undisturbed by the outflow. This has important consequences for AGN feedback models in galaxies. Specifically, this shows that outflows such as the one in Mrk 573 are not strong enough to remove material from the host galaxy; in fact, analyses of low luminosity AGN indicate that AGN feedback has little influence over the host (Krongold et al. 2007; Whittle et al. 2002, 2005, 2009). As feedback is frequently invoked to explain different aspects of host-AGN evolution, new models must take into account that feedback, at least for AGN comparable to local Seyferts, has a significantly smaller effect on the host than previously thought.

We would like to thank Mark Whittle for useful discussions. Support for this work was provided by NASA through grant number GO-9143 from the Space Telescope Science Institute, which is operated by the Association of Universities for Research in Astronomy, Inc., under NASA contract NAS5-26555.

REFERENCES

- Allen, M. G., Dopita, M. A. & Tsvetanov, Z. I. 1998, *ApJ*, 493, 571
- Allen, M. G., Groves, B. A., Dopita, M. A., Sutherland, R. S. & Kewley, L. J. 2008, *ApJS*, *accepted*, ArXiv e-prints, 0805.0204
- Begelman, M. C. 2004, in *Coevolution of Black Holes and Galaxies*, ed. L.C. Ho, 374
- Bell, E. F., Wolf, C., Meisenheimer, K., Rix, H.-W., Borch, A., Dye, S., Kleinheinrich, M., Wisotzki, L. & McIntosh, D. H. 2004, *ApJ*, 608, 752
- Benson, A. J., Bower, R. G., Frenk, C. S., Lacey, C. G., Baugh, C. M. & Cole, S. 2003, *ApJ*, 599, 38
- Bicknell, G. V., Dopita, M. A., Tsvetanov, Z. I. & Sutherland, R. S. 1998, *ApJ*, 495, 680
- Bower, R. G., Benson, A. J., Malbon, R., Helly, J. C., Frenk, C. S., Baugh, C. M., Cole, S. & Lacey, C. G. 2006, *MNRAS*, 370, 645
- Cai, W. & Pradhan, A. K. 1993, *ApJS*, 88, 329
- Crenshaw, D. M., Kraemer, S. B., Boggess, A., Maran, S. P., Mushotzky, R. F. & Wu, C.-C. 1999, *ApJ*, 516, 750

- Crenshaw, D. M., Kraemer, S. B., Hutchings, J. B., Bradley, L. D., Gull, T. R., Kaiser, M. E., Nelson, C. H., Ruiz, J. R. & Weistrop, D. 2000, *AJ*, 120, 1731
- Crenshaw, D. M., Kraemer, S. B. & George, I. M. 2003, *ARA&A*, 41, 117
- Croton, D. J., Springel, V., White, S. D. M., De Lucia, G., Frenk, C. S., Gao, L., Jenkins, A., Kauffmann, G., Navarro, J. F. & Yoshida, N. 2006, *MNRAS*, 365, 11
- Dai, X., Mathur, S., Chartas, G., Nair, S. & Garmire, G. P. 2008, *AJ*, 135, 333
- Das, V., Crenshaw, D. M., Hutchings, J. B., Deo, R. P., Kraemer, S. B., Gull, T. R., Kaiser, M. E., Nelson, C. H. & Weistrop, D. 2005, *AJ*, 130, 945
- Dopita, M. A. 2002, in *Revista Mexicana de Astronomia y Astrofisica Conference Series*, 177
- Fabian, A. C. 1999, *MNRAS*, 308, L39
- Falcke, H., Wilson, A. S. & Simpson, C. 1998, *ApJ*, 502, 199
- Ferrarese, L. & Merritt, D. 2000, *ApJ*, 539, L9
- Ferruit, P., Wilson, A. S., Falcke, H., Simpson, C., Pécontal, E. & Durret, F. 1999, *MNRAS*, 309, 1
- Gebhardt, K. et al. 2000, *ApJ*, 539, L13
- Granato, G. L., De Zotti, G., Silva, L., Bressan, A. & Danese, L. 2004, *ApJ*, 600, 580
- Groves, B. A., Dopita, M. A. & Sutherland, R. S. 2004, *ApJS*, 153, 9
- Kauffmann, G., White, S. D. M., Heckman, T. M., Ménard, B., Brinchmann, J., Charlot, S., Tremonti, C. & Brinkmann, J. 2004, *MNRAS*, 353, 713
- Kim Quijano, J., et al. 2003, "STIS Instrument Handbook", Version 7.0, (Baltimore: STScI).
- Krongold, Y., Nicastro, F., Elvis, M., Brickhouse, N., Binette, L., Mathur, S. & Jiménez-Bailón, E. 2007, *ApJ*, 659, 1022
- Marconi, A. & Hunt, L.K. 2003, *ApJ*, 589, L21
- Martini, P., Pogge, R. W., Ravindranath, S. & An, J. H. 2001, *ApJ*, 562, 139
- Martini, P., Regan, M. W., Mulchaey, J. S., & Pogge, R. W., 2003, *ApJ*, 589, 774
- Osterbrock, D. E. 1989, "Astrophysics of gaseous nebulae and active galactic nuclei", University Science Books
- Pogge, R. W. & de Robertis, M. M. 1993, *ApJ*, 404, 563

- Pogge, R. W. & de Robertis, M. M. 1995, *ApJ*, 451, 585
- Pogge, R. W. & Martini, P., 2002, *ApJ*, 569, 624
- Quillen, A. C., Alonso-Herrero, A., Rieke, M. J., McDonald, C., Falcke, H. & Rieke, G. H. 1999, *ApJ*, 525, 685
- Rice, M. S., Martini, P., Greene, J. E., Pogge, R. W., Shields, J. C., Mulchaey, J. S. & Regan, M. W. 2006, *ApJ*, 636, 654
- Silk, J. & Rees, M. J. 1998, *A&A*, 331, L1
- Springel, V. 2000, *MNRAS*, 312, 859
- Springel, V., Di Matteo, T. & Hernquist, L. 2005, *MNRAS*, 361, 776
- Springel, V., Di Matteo, T. & Hernquist, L. 2005, *ApJ*, 620, L79
- Strateva, I., et al. 2001, *AJ*, 122, 1861
- White, S. D. M. & Frenk, C. S. 1991, *ApJ*, 379, 52
- Whittle, M., Wilson, A. S., Nelson, C. H., Rosario, D. & Silverman, J. D. 2002, in *Revista Mexicana de Astronomia y Astrofisica Conference Series*, 230
- Whittle, M., Rosario, D. J., Silverman, J. D., Nelson, C. H. & Wilson, A. S. 2005, *AJ*, 129, 104
- Whittle, M., Silverman, J. D., Rosario, D. J., Nelson, C. H. & Wilson, A. S. 2009, to appear in *AJ*
- Wilson, A. S. & Tsvetanov, Z. I. 1994, *AJ*, 107, 1227

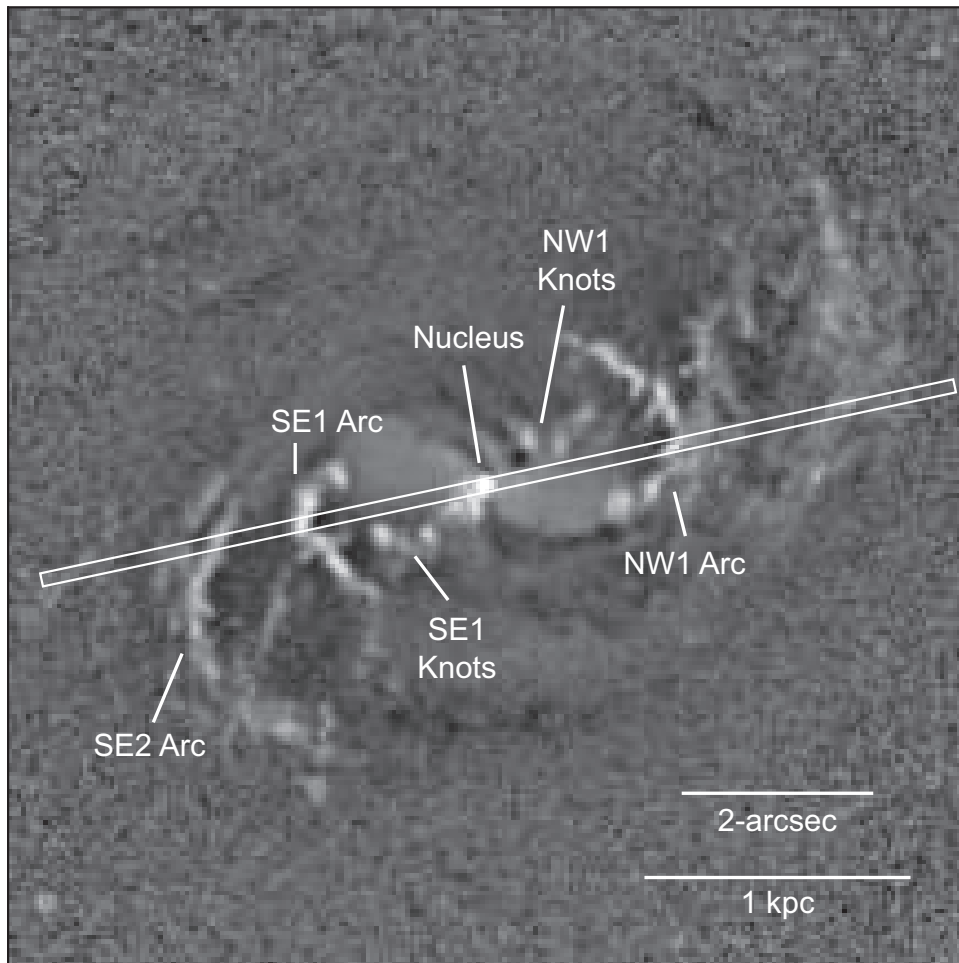


Fig. 1.— Contrast-enhanced structure map of the central $10''$ of Mrk 573, constructed from an archival WFPC2 F606W filter image by Pogge & Martini (2002). Emission-line regions appear bright and dust lanes appear dark. The STIS slit used for the long-slit spectra shown in Figure 2 is superimposed (the actual long slit extends $54''$, but we show only the inner $10''$). The main emission-line regions are labeled with the names adopted from Ferruit et al. (1999). The image is oriented North up, East to the left, with scale bars indicating the angular and approximate linear scales in arcseconds and kiloparsecs, respectively.

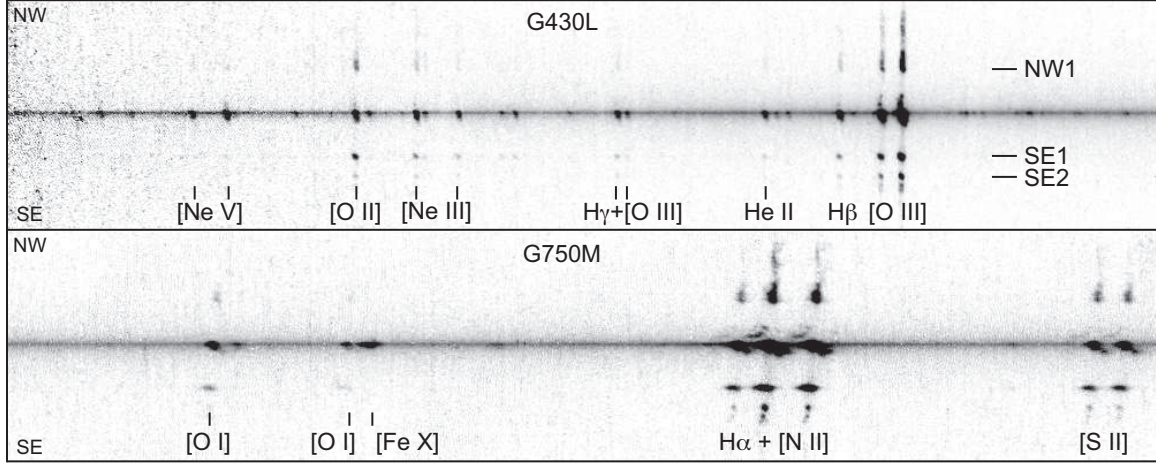


Fig. 2.— Long-slit 2D STIS spectra of Mrk 573 taken with the G430L (*top*) and G750M (*bottom*) gratings. The central $10''$ of the STIS slit is shown, with NW at the top and SE at the bottom of each panel. The G430L spectrum extends from $\lambda 2900\text{\AA}$ to $\lambda 5700\text{\AA}$, while the G750M spectrum extends from $\lambda 6300\text{\AA}$ to $\lambda 6850\text{\AA}$. Prominent emission lines are labeled.

Table 1. Line Flux Measurements

Feature	NW 1	NUC	SE 1	SE 2
Aperture Area (arcsec ²)	0.051	0.061	0.041	0.041
[Ne V] $\lambda 3426\text{\AA}$	5.59e-17	3.40e-15	4.04e-17	5.16e-17
[O II] $\lambda 3727\text{\AA}$	3.11e-16	1.51e-15	7.09e-16	1.28e-16
[Ne III] $\lambda 3868\text{\AA}$	1.17e-16	1.73e-15	2.42e-16	5.75e-17
[Ne III] $\lambda 3968\text{\AA}$	3.76e-17	7.80e-16	1.37e-16	3e-17
H γ $\lambda 4340\text{\AA}$	5.07e-17	8.48e-16	1.03e-16	3.98e-17
[O III] $\lambda 4363\text{\AA}$	1.10e-17	4.22e-16	3.47e-17	5.90e-18
He II $\lambda 4686\text{\AA}$	2.87e-17	8.96e-16	5.33e-17	1.63e-17
H β $\lambda 4861\text{\AA}$	1.08e-16	1.85e-15	2.53e-16	7.24e-17
[O III] $\lambda 4959\text{\AA}$	4.70e-16	7.94e-15	9.58e-16	3.10e-16
[O III] $\lambda 5007\text{\AA}$	1.29e-15	2.37e-14	2.80e-15	8.98e-16
[O I] $\lambda 6300\text{\AA}$	5.32e-17	5.37e-16	1.02e-16	1.81e-17
H α $\lambda 6563\text{\AA}$	4.48e-16	7.14e-15	9.76e-16	2.58e-16
[N II] $\lambda 6583\text{\AA}$	4.32e-16	3.57e-15	9.62e-16	1.21e-16
[S II] $\lambda 6716\text{\AA}$	1.28e-16	6.29e-16	2.69e-16	4.81e-17
[S II] $\lambda 6731\text{\AA}$	1.31e-16	8.64e-16	3.24e-16	4.3e-17

Note. — The line flux measurements for the four emission-line regions in Mrk 573. The fluxes have the units $\text{erg s}^{-1} \text{cm}^{-2}$ and uncertainties of 20% or less.

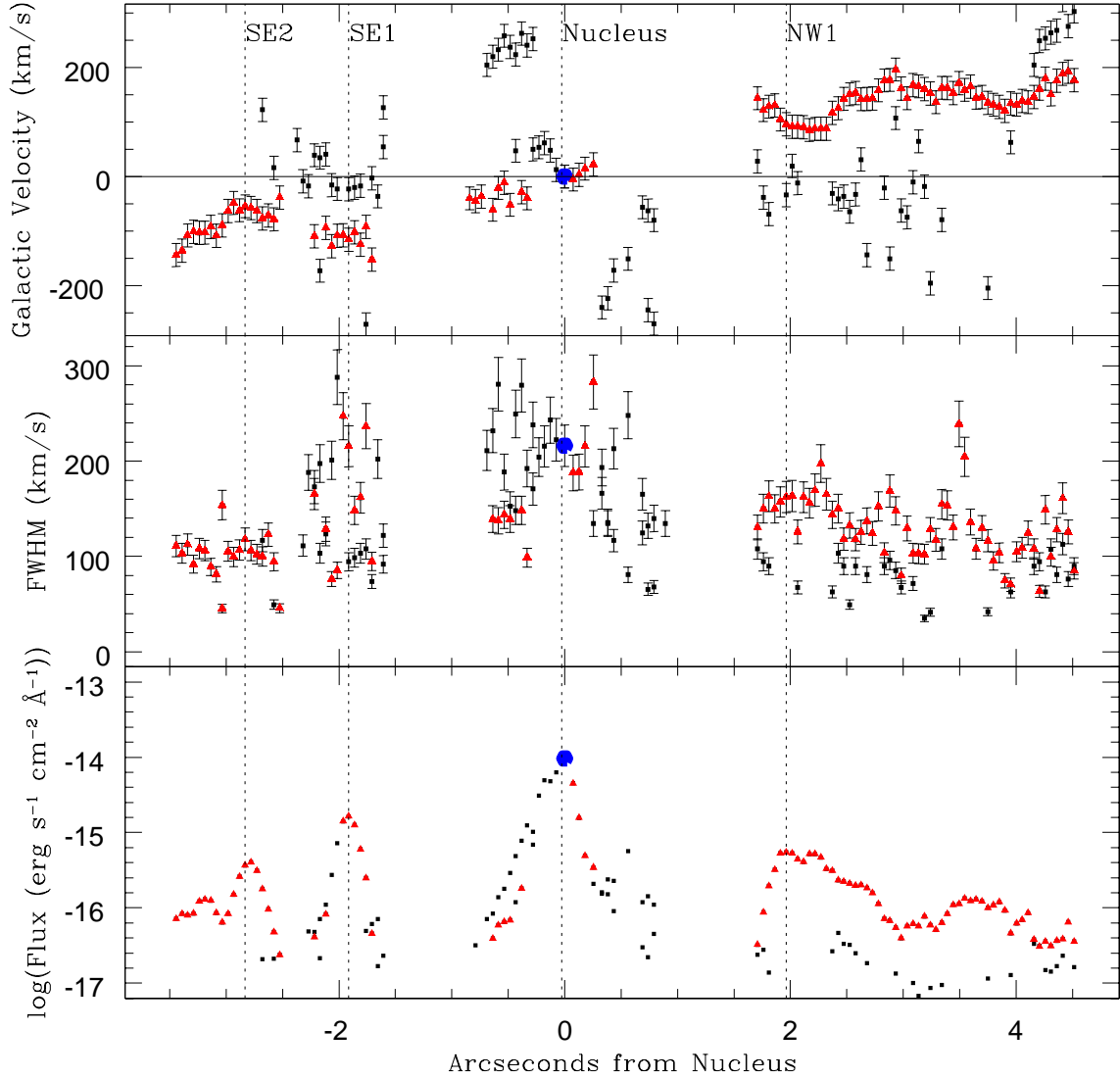


Fig. 3.— The H α radial velocity profile (*top*), FWHM profile (*middle*), and total line intensity profile (*bottom*) along our slit for Mrk 573 as a function of distance from the nucleus. The red triangles represent rotating disk component, the black squares correspond to the biconical outflow region, and the large blue filled circle represents the nucleus. The centroids of the individual emission line regions are marked by the dotted vertical lines.

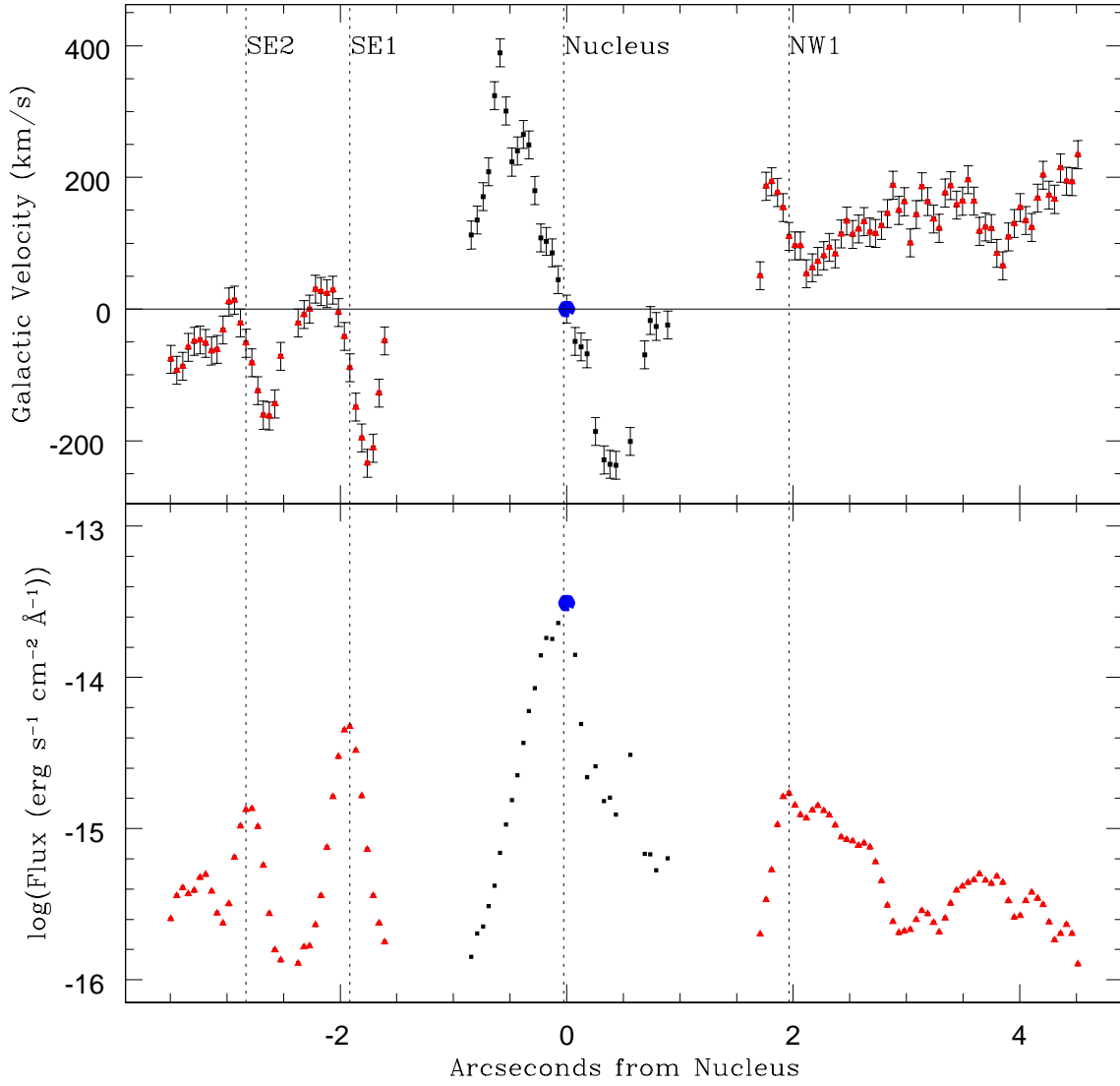


Fig. 4.— Same as Figure 3 for the $[\text{O III}] \lambda 5007\text{\AA}$ emission line. The FWHM curve is not shown as the resolution of the G430L grating is low dispersion, resulting in broader features.

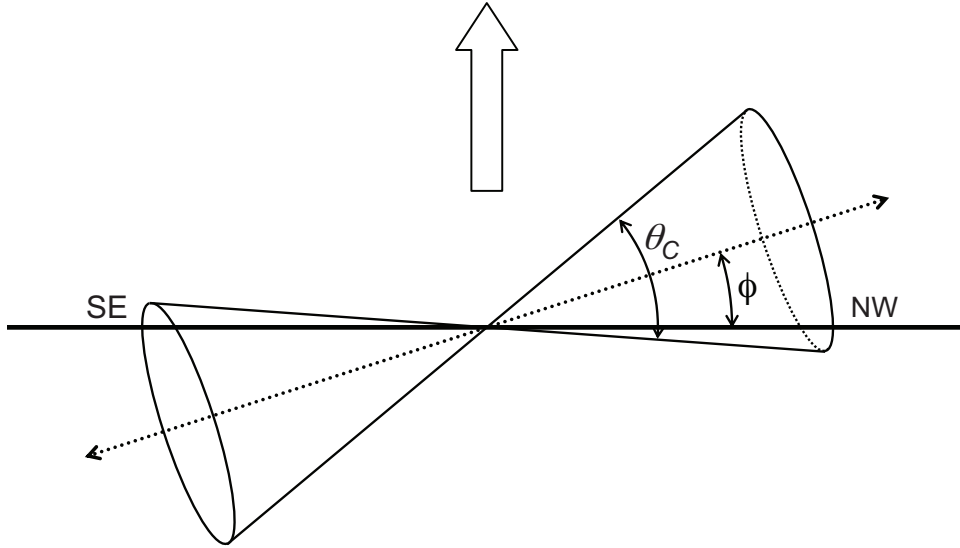


Fig. 5.— Schematic of the inferred outflow geometry viewed perpendicular to the line of sight towards Earth (indicated by the large arrow). This view is from the south looking towards the nucleus. The ionization cone is shown with the 45° opening angle (θ_C) measured by Wilson & Tsvetanov (1994) and is tilted by angle 18° (ϕ) with respect to the plane of the sky, as estimated from our kinematics (see section 3.1). In this geometry, the NW outflow is emerging out of the plane of the sky towards us, while the SE flow is going into the sky.

Table 2. Density and Temperature Regional Analysis

Feature	NW 1	NUC	SE 1	SE 2
$\frac{H\gamma}{H\beta}$	0.471 ± 0.13	0.458 ± 0.13	0.407 ± 0.11	0.549 ± 0.15
$\frac{\lambda\lambda 4959+5007}{4363}_{obs}$	160.42 ± 54	74.96 ± 25	108.36 ± 36	204.90 ± 69
$\frac{\lambda\lambda 4959+5007}{4363}_{corr}$	160.59 ± 54	77.17 ± 26	125.53 ± 42	-
$\frac{\lambda 6716}{\lambda 6731}$	0.979 ± 0.27	0.728 ± 0.20	0.828 ± 0.23	0.981 ± 0.27
n_e (cm^{-3})	789 ± 78	2437 ± 243	1489 ± 148	762 ± 76
T_e (K)	10814 ± 1081	14454 ± 1445	12445 ± 1244	10046 ± 1004

Note. — The line ratios and derived densities and temperatures for the four extraction regions. The Balmer decrement for SE 2 was non-physical for the specified temperature, so we assume that the reddening is negligible. The uncertainties for the density and temperature are 10%.

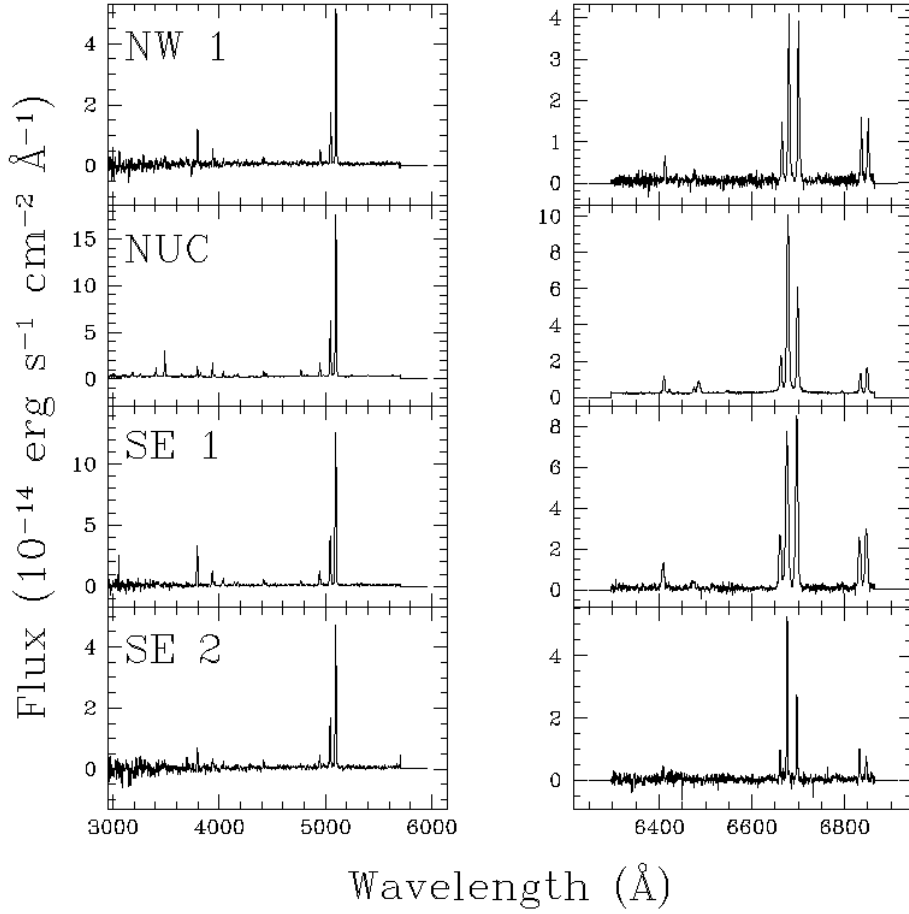


Fig. 6.— Extracted spectra of emission-line regions in Mrk 573. The left panels contain the G430L spectra and are labeled with the associated region from Figure 1. The right panels contains the G750M spectra. Each extraction region was chosen to include all of the emission of each region; the angular extent of these regions is listed in Table 1. All of the regions have [O III] $\lambda\lambda$ 4363, 4959, and 5007 Å and [S II] $\lambda\lambda$ 6716 and 6731 Å emission features, which were used to determine the density and temperature. The nucleus includes additional high-ionization features, such as [Fe X] λ 6375 Å which indicates the presence of close-in material at higher temperatures.

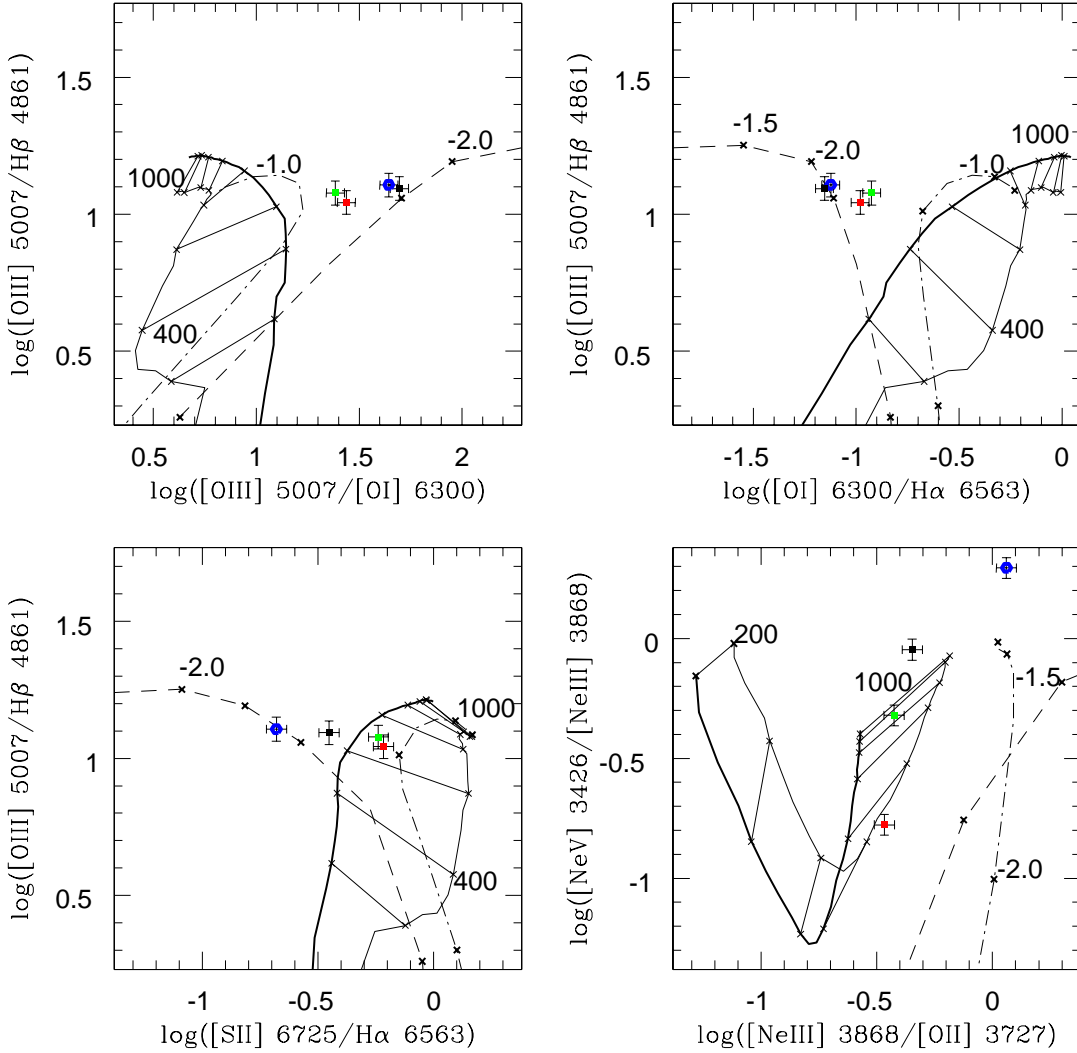


Fig. 7.— Optical ionization diagnostic diagrams. These diagnostics are the best at distinguishing between shocked and photoionized regions. Inconclusive ionization diagnostics are not included, but are available by request. The dashed line is $U_{1.4}$, photoionization of an optically thick medium by power-law emission. The crosses mark $\log U_{1.4} = -1.0, -1.5, -2.0, -2.5$ and -3.5 . The dot-dash line represents U_{dust} , power-law photoionized dusty gas. Crosses mark $\log U_{dust} = -3.0, -2.0, -1.0$, and 0.0 . The solid lines represent shocks from Allen et al. (2008). The thin line is a photoionizing shock with $B/\sqrt{n} \approx 0 \mu\text{G cm}^{-3/2}$. The thicker solid line connected to the thin is a photoionizing shock with $B/\sqrt{n} = 10 \mu\text{G cm}^{-3/2}$. These two shocks are modeled for velocities of 200–1000 km s^{-1} . The crosses mark every additional 100 km s^{-1} . These models are shocks and precursors and assume a pre-shock density of 1 cm^{-3} and solar abundance. The points represent each of the four studied regions of Markarian 573. Blue represents the nucleus, green is the NW1 region, and red and black are SE1 and SE2, respectively.

Table 3. Emission Measure Analysis

	Temperature (K)	B_{NW}	B_{SE}
$I(H\beta)$ ($\text{erg s}^{-1} \text{cm}^{-2} \text{arcsec}^{-2}$)	-	4.1e-16	2.4e-16
Depth (arcsec)	-	1.6	1.6
Depth (parsec)	-	576	576
Emission Measure ($\text{cm}^{-6} \text{pc}$)	15000	826	483
$\langle n_e \rangle$ (cm^{-3})	15000	1.2	0.9
Emission Measure ($\text{cm}^{-6} \text{pc}$)	10^6	36210	21197
$\langle n_e \rangle$ (cm^{-3})	10^6	7.9	6.1

Note. — Temperature and density calculations from the emission measure for the bubble regions as described in section 3.2.2. B_{NW} refers to the bubble between NW1 and the nucleus and B_{SE} between the nucleus and SE 1.

Table 4. Quantitative Analysis of the Outflow Arcs

Quantity	Symbol (units)	NW 1	NUC	SE 1	SE 2
Region Angular Size (x)	θ_{ex} (arcsec)	2.14±0.1	0.67±0.1	2.55±0.1	3.72±0.1
Region Angular Size (y)	θ_{ey} (arcsec)	0.31±0.1	0.31±0.1	0.26±0.1	0.31±0.1
Distance from Nucleus	Δ_e (arcsec)	1.81±0.1	-	1.76±0.1	2.63±0.1
Electron Temperature	T_e (K)	10814±1081	14454±1445	12445±1244	10046±1004
Electron Density	n_e (cm^{-3})	789±78	2437±243	1489±148	762±76
H β Emission Flux	$\log(F_{H\beta})$ ($erg\ s^{-1}\ cm^{-2}$)	-14.8±0.1	-14.0±0.1	-14.4±0.1	-14.9±0.1
[O III] λ 5007 Emission Flux	$\log(F_{5007})$ ($erg\ s^{-1}\ cm^{-2}$)	-13.7±0.1	-12.9±0.1	-13.4±0.1	-13.9±0.1
Emission-line Width	$W_{em,H\alpha}$ (km/s)	159±20	217±20	214±20	108±20
Emission-line Velocity	$V_{em,H\alpha}$ (km/s)	110±20	-	-83±20	-62±20
Emission Mass	M_{em} ($10^6 M_{\odot}$)±22%	0.009	0.018	0.012	0.007
Emission Region Age	t_{em} (Myr)	2.24±0.65	-	3.53±1.31	6.90±2.50
Emission Luminosity	$\log(L_{em})$ (erg/s)	41.1±0.1	41.9±0.1	41.4±0.1	40.9±0.1
Emission Region Energy	$\log(E_{em})$ (erg)	54.97±0.15	-	55.46±0.18	55.26±0.18
Emission Region Momentum	$\log(G_{em})$ ($gm\ cm\ s^{-1}$)	44.81±0.15	-	44.81±0.18	44.45±0.18
Emission Region Force	$\log(\Pi_{em})$ (dyne)	30.96±0.22	-	30.76±0.26	30.11±0.26
Thermal Energy	$\log(E_{th})$ (erg)	49.60±0.10	50.03±0.10	49.79±0.10	49.46±0.10
Transverse Kinetic Energy	$\log(E_{kin,t})$ (erg)	52.06±0.15	-	51.94±0.18	51.45±0.18
Internal Kinetic Energy	$\log(E_{kin,i})$ (erg)	50.61±0.10	-	51.00±0.10	50.17±0.10
Total Mechanical Energy	$\log(E_{mec})$ (erg)	52.07±0.18	-	51.99±0.20	51.47±0.20
Photon Energy	$\log(E_{ph})$ (erg)	55.6±0.1	-	55.9±0.2	56.1±0.2
Relativistic Energy	$\log(E_{rel})$ (erg)	≈52±0.17	-	≈53±0.17	-
Emission Region Pressure	$\log(P_{em})$ ($dyne\ cm^{-2}$)	-8.92±0.04	-8.31±0.04	-8.59±0.04	-8.97±0.04
Radiation Pressure	$\log(P_{rad})$ ($dyne\ cm^{-2}$)	-10.5±0.06	-	-10.5±0.06	-10.9±0.04
Relativistic Pressure	$\log(P_{rel})$ ($dyne\ cm^{-2}$)	-8.0±0.14	-	-7.6±0.14	-
Outflow Ram Pressure	$\log(P_{o,dyn})$ ($dyne\ cm^{-2}$)	-10.9±.22	-	-11.1±.26	-
Outflow Speed	V_o (km/s)	340±228	-	1700±1207	-
Outflow Mach Number	N_{Ma}	0.03±0.5	-	0.01±0.5	-
Magnetic Field Strength	$\log(B_{min})$ (Gauss)	-3.25±0.07	-	-3.05±0.07	-
IRAS 60 μ m Flux	S_{60} (Jy)		1.27±0.15		
IRAS 100 μ m Flux	S_{100} (Jy)		1.26±0.16		

Note. — A quantitative analysis of Mrk 573 calculated based upon the formulations of Whittle et al. (2009). These quantities are derived in section 4. Uncertainties are calculated using standard error propagation.